

# We are IntechOpen, the world's leading publisher of Open Access books Built by scientists, for scientists

6,900

Open access books available

185,000

International authors and editors

200M

Downloads

Our authors are among the

154

Countries delivered to

TOP 1%

most cited scientists

12.2%

Contributors from top 500 universities



WEB OF SCIENCE™

Selection of our books indexed in the Book Citation Index  
in Web of Science™ Core Collection (BKCI)

Interested in publishing with us?  
Contact [book.department@intechopen.com](mailto:book.department@intechopen.com)

Numbers displayed above are based on latest data collected.  
For more information visit [www.intechopen.com](http://www.intechopen.com)



# InSAR Modeling of Geophysics Measurements

*Andon Lazarov, Dimitar Minchev and Chavdar Minchev*

## Abstract

In the present work, the geometry and basic parameters of interferometric synthetic aperture radar (InSAR) geophysics system are addressed. Equations of pixel height and displacement evaluation are derived. Synthetic aperture radar (SAR) signal model based on linear frequency modulation (LFM) waveform and image reconstruction procedure are suggested. The concept of pseudo InSAR measurements, interferogram, and differential interferogram generation is considered. Interferogram and differential interferogram are generated based on a surface model and InSAR measurements. Results of numerical experiments are provided.

**Keywords:** InSAR, geometry, signal modeling, SAR interferogram, SAR differential interferograms

## 1. Introduction

Synthetic aperture radar (SAR) is a coherent microwave imaging instrument capable to provide for data all weather, day and night, guaranteeing global coverage surveillance. SAR interferometry is based on processing two or more complex valued SAR images obtained from different SAR positions [1–4]. The InSAR is a system intends for geophysical measurements and evaluation of topography, slopes, surface deformations (volcanoes, earthquakes, ice fields), glacier studies, vegetation growth, etc. The estimation of topographic height with essential accuracy is performed by the interferometric distance difference measured based on two SAR echoes from the same surface. Changes in topography (displacement), precise to a fraction of a radar wavelength, can be evaluated by differential interferogram generated by three or more successive complex SAR images [5, 6]. Demonstration of time series InSAR processing in Beijing using a small stack of Gaofen-3 differential interferograms is discussed in [7].

A general overview of the InSAR principles and the recent development of the advanced multi-track InSAR combination methodologies, which allow to discriminate the 3-D components of deformation processes and to follow their temporal evolution, are presented in [8]. The combination of global navigation satellite system (GNSS) and InSAR for future Australian datums is discussed in [9].

A high-precision DEM extraction method based on InSAR data and quality assessment of InSAR DEMs is suggested in [10, 11]. InSAR digital surface model (DSM) and time series analysis based on C-band Sentinel-1 TOPS data are presented in [12, 13]. DEM registration, alignment, and evaluation for SAR interferometry, deformation monitoring by ground-based SAR interferometry (GB-InSAR), a field

test in dam, and an improved approach to estimate large-gradient deformation using high-resolution TerraSAR-X data are discussed in [14–16]. *InSAR Time-Series Estimation of the Ionospheric Phase Delay: An Extension of the Split Range-Spectrum Technique* and InSAR data coherence estimation using 2D fast Fourier transform are performed in [17, 18].

In comparison with the results described in the aforementioned publications, the main goal of the present work is to suggest an analytical model of multi-pass InSAR geometry and derive analytical expressions of current distances between SAR's positions and individual pixels on the surface and to describe principal InSAR parameters: topographic height and topographic displacement from the position of InSAR modelling. The focus is on the two modelling approaches: first, by the definition of real scenario, geometry, and kinematics and SAR signal models and corresponding complex image reconstruction and interferogram and differential interferogram generation and, second, the process of pseudo SAR measurements and interferogram generation that is analytically described. Results of numerical experiments with real data are provided.

The rest of the chapter is organized as follows. In Section 2, 3D InSAR geometry and kinematics are analytically described. In Section 3 and Section 4, analytical expressions of InSAR relief measurements and relief displacement measurements are presented. In Section 5 and Section 6, SAR waveform, deterministic signal model, and image reconstruction algorithm are described. In Section 7, numerical results of InSAR modelling based on the geometry, kinematics, and signal models are provided. In Section 8 and Section 9, a pseudo InSAR modelling of geophysical measurements and numerical results are presented, respectively. Conclusion remarks are made in Section 10.

## 2. InSAR geometry and kinematics

Assume a three-pass SAR system viewing three-dimensional (3-D) surface presented by discrete resolution elements, pixels. Each pixel is defined by the third coordinate  $z_{ij}(x_{ij}, y_{ij})$  in 3-D coordinate system Oxyz. Let A, B, and C, be the SAR positions of imaging. Between every SAR position,  $C_3^2 = 3$  InSAR baselines can be drawn.

The basic geometric SAR characteristic is the time-dependent distance vector from SAR to each pixel on the surface in the  $n$ -th SAR pass at the  $p$ -th moment defined by

$$R_{ij}^n(p) = R^n(p) - R_{ij} = [x_{ij}^n(p), y_{ij}^n(p), z_{ij}^n(p)]^T, \quad (1)$$

where  $n = 1-3$  is the number of SAR passes and  $R^n(p) = R^{0n} + V \cdot p \cdot T_p$  is the distance vector in the  $n$ -th SAR pass at the  $p$ -th moment,  $R^{0n}$  is the initial distance vector in the  $n$ -th SAR pass,  $R_{ij}$  is the constant distance vector of the  $ij$ -th pixel on the surface, and  $x_{ij}^n(p)$ ,  $y_{ij}^n(p)$ , and  $z_{ij}^n(p)$  are the current coordinates of  $R_{ij}^n(p)$  written by the expression.

$$x_{ij}^n(p) = x^n(p) - x_{ij}, y_{ij}^n(p) = y^n(p) - y_{ij}, z_{ij}^n(p) = z^n(p) - z_{ij} \quad (2)$$

where  $x_{ij} = i\Delta X$ ,  $y_{ij} = j\Delta Y$ , and  $z_{ij} = z_{ij}(x_{ij}, y_{ij})$  is the pixel's discrete coordinates and  $x^n(p)$ ,  $y^n(p)$ , and  $z^n(p)$  are the SAR current coordinates in the  $n$ -th pass, defined by the following equation.

$$x^n(p) = x_0^n - V_x p T_p, y^n(p) = y_0^n - V_y p T_p, z^n(p) = z_0^n - V_z p T_p, \quad (3)$$

where  $x_0^n$ ,  $y_0^n$ , and  $z_0^n$  are the SAR initial coordinates in the  $n$ -th pass, measured at the initial moment;  $T_p$  is the time repetition period;  $p$  is the number of the emitted pulse;  $V = [V_x, V_y, V_z]^T$  is the SAR vector velocity;  $V_x = V \cos \alpha$ ,  $V_y = V \cos \beta$ , and  $V_z = V \cos \delta$  are the components of vector velocity;  $\cos \alpha$ ,  $\cos \beta$ , and  $\cos \delta = \sqrt{1 - \cos^2 \alpha - \cos^2 \beta}$  are the guiding cosines; and  $V$  is the module of the vector velocity  $V$ . Modulus of the current distance vector  $R_{ij}^n(p)$  is defined by

$$R_{ij}^n(p) = \left\{ \left[ x_{ij}^n(p) \right]^2 + \left[ y_{ij}^n(p) \right]^2 + \left[ z_{ij}^n(p) \right]^2 \right\}^{\frac{1}{2}}. \quad (4)$$

Eq. (4) can be used to model a SAR signal from the  $ij$ -th pixel in the  $n$ -th SAR pass by calculation of the respective time delay and phase of the signal.

### 3. InSAR relief measurements

The distances to  $ij$ -th pixel from SAR in  $m$ -th and  $n$ -th pass ( $m \neq n$ ) at the moment of imaging can be defined by the cosine's theorem, i.e.,

$$\left| R_{ij}^n \right| = \left\{ \left| R_{ij}^m \right|^2 + B_{mn}^2 - 2 B_{mn} \left| R_{ij}^m \right| \cos \left[ \frac{\pi}{2} - [\theta^{m_{ij}} - \alpha_{mn}] \right] \right\}^{\frac{1}{2}}, \quad (5)$$

where  $B_{mn}$  is the modulus of the baseline vector,  $\theta^{m_{ij}}$  is the look angle, and  $\alpha_{mn}$  is a priori known tilt angle, the angle between the baseline vector and plane  $Oxy$ . The look angle  $\theta^{m_{ij}}$  and height  $h^m$  of an  $ij$ -th pixel on the surface with respect to  $m$ -th SAR position in the moment of imaging can be written as

$$\theta^{m_{ij}} = \alpha_{mn} + \arcsin \frac{\left| R_{ij}^m \right|^2 + B_{mn}^2 - \left| R_{ij}^n \right|^2}{2 B_{mn} \left| R_{ij}^m \right|}, \quad (6)$$

$$z_{ij} = h^m - \left| R_{ij}^m \right| \cos \theta^{m_{ij}}. \quad (7)$$

The distance difference,  $\left| \Delta R_{ij}^{mn} \right| = \left| R_{ij}^n \right| - \left| R_{ij}^m \right|$ , can be expressed by the interferometric phase difference  $\left| \Delta R_{ij}^{mn} \right| = \frac{\lambda}{2\pi} \Delta \phi_{ij}^{mn}$ . In case  $\left| R_{ij}^m \right|$  can be measured, i.e.,

$\left| R_{ij}^n \right| = \left| R_{ij}^m \right| + \left| \Delta R_{ij}^{mn} \right|$ , then

$$\theta^{m_{ij}} = \alpha_{mn} + \arcsin \left[ \frac{B_{mn}}{2 R_{ij}^m} - \frac{\lambda}{2\pi B_{mn}} \Delta \phi_{ij}^{mn} \left( 1 + \frac{\lambda}{4\pi R_{ij}^m} \Delta \phi_{ij}^{mn} \right) \right], \quad (8)$$

$$z_{ij} = h^m - R_{ij}^m \cdot \cos \left\{ \alpha_{mn} + \arcsin \left[ \frac{B_{mn}}{2 R_{ij}^m} - \frac{\lambda}{2\pi B_{mn}} \Delta \phi_{ij}^{mn} \cdot \left( 1 + \frac{\lambda}{4\pi R_{ij}^m} \Delta \phi_{ij}^{mn} \right) \right] \right\}. \quad (9)$$

#### 4. InSAR measurements of relief displacement

Consider a three-pass SAR interferometry (**Figure 1**). Let A and B be the two positions of imaging which can be defined by two passes of the same spaceborne SAR in different time (two pass interferometry). The third position C is defined by the third pass of the spaceborne SAR. The surface displacement,  $\Delta z_{ij}$ , due, for instance, to an earthquake could derive from two SAR interferograms built before and after the seismic impact. The temporal baseline, the time scale over which the displacement is measured, must follow the dynamics of the geophysical phenomenon. Short-time baseline is applied for monitoring fast surface changes. Long temporal baseline is used for monitoring slow geophysics phenomena (subsidence). The interferometry phase before event is derived from complex images acquired by A and B SAR positions in the moment of imaging, while the interferometry phase after event is derived from complex images acquired by A and C SAR positions in the moment of imaging. The distances  $R_{ij}^1$ ,  $R_{ij}^2$ ,  $R_{ij}^3$ , and  $R_{ij}^{d3}$  after standard manipulations are written as.

$$R_{ij}^2 \simeq R_{ij}^1 - B_1 \sin(\theta_{ij} - \alpha_1) + \frac{B_1^2}{2R_{ij}^1}, R_{ij}^3 \simeq R_{ij}^1 - B_2 \sin(\theta_{ij} - \alpha_2) + \frac{B_2^2}{2R_{ij}^1}, \quad (10)$$

$$R_{ij}^{d3} \simeq R_{ij}^3 - \Delta z \left( \cos \theta_{ij} + \frac{B_2}{R_{ij}^1} \sin \alpha_2 \right) + \frac{(\Delta z_{ij})^2}{2R_{ij}^1},$$

where  $R_{ij}^1$ ,  $R_{ij}^2$ , and  $R_{ij}^3$  are the slant ranges from A, B, and C positions of SAR system to the observed pixel in the moment of imaging before the surface

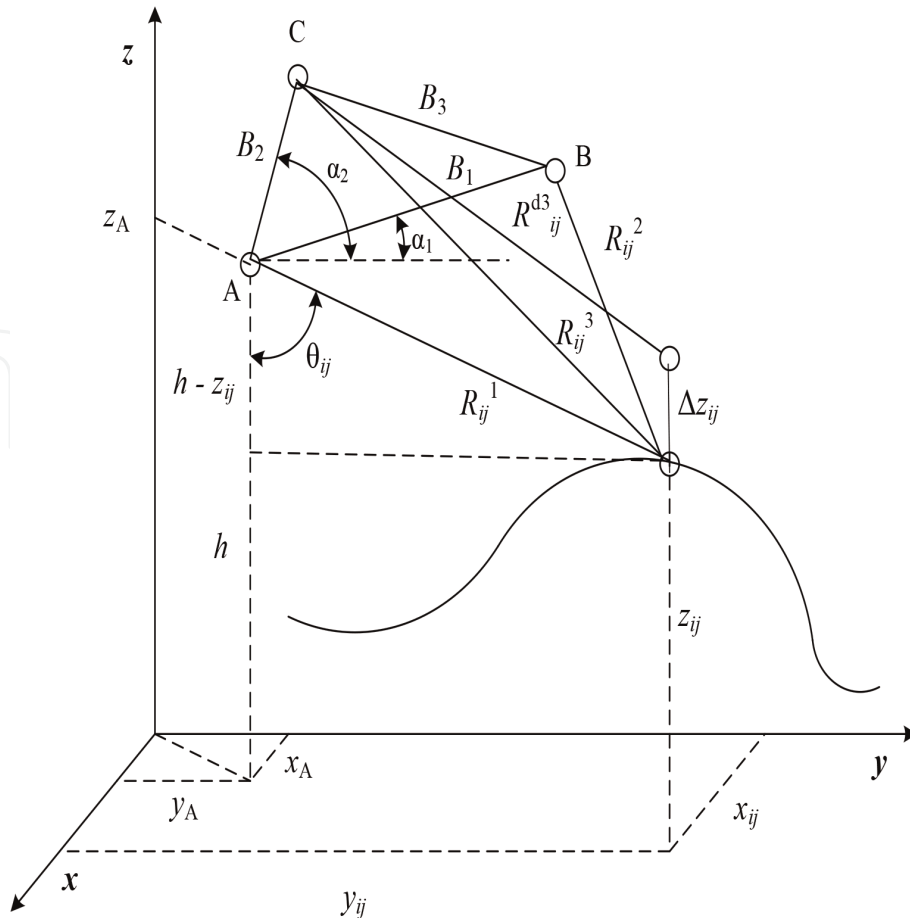


**Figure 1.**  
InSAR geometry and kinematics.

displacement and  $R_{ij}^{d3}$  is the slant range to from C SAR position to the observed pixel after  $\Delta z_{ij}$  surface displacement.

Given the SAR wavelength  $\lambda$ , the phase differences proportional to range differences related to a particular pixel before and after displacement in the moment of imaging can be written as.

$$\phi^{AB} = \frac{4\pi}{\lambda} (R_{ij}^1 - R_{ij}^2), \phi^{AC} = \frac{4\pi}{\lambda} (R_{ij}^1 - R_{ij}^3), \phi_d^{AC} = \frac{4\pi}{\lambda} (R_{ij}^1 - R_{ij}^{d3}) \quad (11)$$

Neglecting the term  $(\Delta z)^2/2R_{ij}^1$  in Eq. (10) can be rewritten as.

$$\phi^{AB} = \frac{4\pi}{\lambda} \left( B_1 \sin(\theta_{ij} - \alpha_1) - \frac{B_1^2}{2R_{ij}^1} \right); \phi^{AC} = \frac{4\pi}{\lambda} \left( B_2 \sin(\theta_{ij} - \alpha_2) - \frac{B_2^2}{2R_{ij}^1} \right) \quad (12)$$

$$\begin{aligned} \phi_d^{AC} = \frac{4\pi}{\lambda} \left[ B_2 \sin(\theta_{ij} - \alpha_2) - \frac{B_2^2}{2R_{ij}^1} + \Delta z \left( \cos \theta_{ij} + \frac{B_2}{R_{ij}^1} \sin \alpha_2 \right) \right] \\ \phi^{AC} + \Delta z \left( \cos \theta_{ij} + \frac{B_2}{R_{ij}^1} \sin \alpha_2 \right) \end{aligned} \quad (13)$$

The displacement  $\Delta z_{ij}$  is extracted from the differential interferometric phase difference  $\Delta \Phi_d = \phi_d^{AC} - \phi^{AB}$ . Considering  $B_2/R_{ij}^1 < 1$ , then  $\Delta \Phi_d = \Delta \Phi + \frac{4\pi}{\lambda} \Delta z_{ij} \cos \theta_{ij}$ , where

$$\Delta \Phi = \frac{4\pi}{\lambda} \left[ B_2 \sin(\theta_{ij} - \alpha_2) - B_1 \sin(\theta_{ij} - \alpha_1) - \frac{B_2^2 - B_1^2}{2R_{ij}^1} \right]. \quad (14)$$

For surface displacement  $z_{ij}$  can be written as

$$\Delta z_{ij} = \frac{\lambda}{4\pi} \frac{\Delta \Phi_d - \Delta \Phi}{\cos \theta_{ij}}. \quad (15)$$

## 5. SAR waveform and deterministic signal model

The SAR transmits a series of electromagnetic waveforms to the surface, which are described analytically by the sequence of linear frequency modulation (chirp) pulses as follows

$$S(t) = \sum_{p=1}^M A \exp \left\{ -j \left[ \omega (t - pT_p) + b (t - pT_p)^2 \right] \right\}, \quad (16)$$

where  $A$  is the amplitude of the transmitted pulses,  $T_p$  is the pulse repetition period,  $\omega = 2\pi c/\lambda$  is the angular frequency,  $p = \overline{1, M}$  is the index of LFM emitted pulse,  $M$  is an emitted pulse number for synthesis of the aperture,  $c = 3 \times 10^8$  m/s is the light speed in vacuum,  $\Delta F$  is the LFM pulse bandwidth,  $b = \pi \Delta F/T$  is the chirp rate, and  $T$  is the time LFM pulse width.

The SAR signal, reflected by  $ij$ -th pixel and registered in the  $n$ -th pass, can be expressed as

$$S_{ij}^n(t) = a_{ij}(z_{ij}) \text{rect} \frac{t - t_{ij}^n}{T} \exp \left\{ -j \left[ \omega(t - t_{ij}^n) + b(t - t_{ij}^n)^2 \right] \right\} \quad (17)$$

$$\text{rect} \frac{t - t_{ij}^n(p)}{T} = \begin{cases} 1, & 0 < \frac{t - t_{ij}^n(p)}{T} \leq 1 \end{cases}, \quad (18)$$

where  $a_{ij}(z_{ij})$  is the reflection coefficient of the pixel from the surface.

The parameter  $a_{ij}(z_{ij})$  is a function of surface geometry;  $t_{ij}^n(p) = \frac{R_{ij}^1(p) + R_{ij}^n(p)}{c}$  is the time propagation of the reflected signal from the  $ij$ -th scattering pixel registered in the  $n$ -th pass.

SAR signal reflected from the entire illuminated surface is an interference of elementary signals of scattering pixels and can be written as

$$S^n(t) = \sum_i \sum_j a_{ij}(z_{ij}) \text{rect} \frac{t - t_{ij}^n}{T} \exp \left\{ -j \left[ \omega(t - t_{ij}^n) + b(t - t_{ij}^n)^2 \right] \right\}. \quad (19)$$

The time dwell  $t$  of the SAR signal return for each transmitted pulse  $p$  can be expressed as  $t = t_{ij\min}^n(p) + k\Delta T$ , where  $k = \overline{k_{ij\min}^n(p), k_{ij\max}^n(p)}$  is the sample number of the SAR return measured on range direction in  $n$ -th pass,  $k_{ij\min}^n = \text{int} \left[ t_{ij\min}^n(p) / \Delta T \right]$ ,  $k_{ij\max}^n = \text{int} \left[ t_{ij\max}^n(p) / \Delta T \right]$ ,  $\Delta T = 1 / (2\Delta F)$  is the sample time width, and  $k_{\max}^n(p)$  is the number of the furthest range bin where SAR signal is registered in  $n$ -th pass. Hence, in discrete form SAR signal can be rewritten as

$$\begin{aligned} \hat{S}^n(k, p) &= \sum_i \sum_j a_{ij}(z_{ij}) \text{rect} \frac{t - t_{ij}^n}{T} \\ &\exp \left\{ -j \left[ \omega((k - 1)\Delta T - t_{ij}^n(p)) + b((k - 1)\Delta T - t_{ij}^n(p))^2 \right] \right\}. \end{aligned} \quad (20)$$

The expressions derived in Section 2 and Section 5 can be used for modeling the SAR signal return in case the satellites are moving rectilinearly in 3-D coordinate system.

## 6. SAR image reconstruction

The complex image reconstruction includes the following operations: frequency demodulation, range compression, coarse range alignment, precise phase correction, and azimuth compression. The frequency demodulation is performed by multiplication of Eq. (20) with a complex conjugated function  $\exp \left\{ j \left( \omega(k - 1)\Delta T + b[(k - 1)\Delta T]^2 \right) \right\}$ .

Thus, the range distributed frequency demodulated SAR return in  $n$ -th pass for  $p$ -th pulse can be written as

$$\hat{S}^n(k, p) = \sum_i \sum_j a_{ij}(z_{ij}) \text{rect} \frac{(k - 1)\Delta T - t_{ij}^n}{T} \cdot \exp \left\{ -j \left[ \omega t_{ij}^n(p) + b((k - 1)\Delta T - t_{ij}^n(p))^2 \right] \right\}. \quad (21)$$

The range compression of the LFM demodulated SAR signal is performed by cross correlation with a reference function,  $\exp \left\{ j b[(k - 1)\Delta T]^2 \right\}$

$$\dot{S}_R^n(\hat{k}, p) = \sum_{k=1}^K \dot{S}^n(k, p) \exp \left\{ j b \left[ (k - \hat{k} - 1) \Delta T \right]^2 \right\} \quad (22)$$

where  $K$  is the full number of LFM samples, the range bins where SAR signal is registered, and by Fourier transform

$$\dot{S}_R^n(\hat{k}, p) = \sum_{k=1}^K \dot{S}^n(k, p) \cdot \exp \left( j \frac{2\pi k \hat{k}}{K_{\max}^n} \right), \quad (23)$$

for each  $p = \overline{1, M}$  and  $\hat{k} = \overline{1, K}$ .

The range alignment and higher-order phase correction are beyond of the scope of the present work. The azimuth compression is accomplished by Fourier transform of the range compressed signal,  $\dot{S}_R^n(\hat{k}, p)$ . The complex image extracted from the  $n$ -th pass data can be expressed as

$$\dot{I}^n(\hat{k}, \hat{p}) = \sum_{p=1}^M \dot{S}_R^n(p, \hat{k}) \exp \left( j \frac{2\pi p \hat{p}}{M} \right), \quad (24)$$

for each  $\hat{p} = \overline{1, M}$ ,  $\hat{k} = \overline{1, K}$ .

The complex SAR image extracted from the  $n$ -th pass data preserves phases defined by distances from the satellite to each pixel at the moment of imaging. Based on pixel phases and image co-registration, a complex interferograms and differential interferograms can be created.

## 7. InSAR modeling: numerical results

The SAR signal model and imaging algorithm are illustrated by results of numerical experiments. Consider three pass satellite SAR system with position coordinates at the moment of imaging as follows.

$$\begin{aligned} x_0^1 &= 0 \text{ m}; y_0^1 = 10.10^3 \text{ m}; z_0^1 = 100.10^3 \text{ m}; x_0^2 = 0 \text{ m}; y_0^2 = 10.1.10^3 \text{ m}; \\ z_0^2 &= 100.10^3 \text{ m}, \\ x_0^3 &= 0 \text{ m}; y_0^3 = 10.2.10^3 \text{ m}; z_0^3 = 100.10^3 \text{ m}. \end{aligned}$$

Coordinates of vector-velocity of the satellite are  $v_x = 0$  m/s,  $v_y = -600$  m/s, and  $v_z = 0$  m/s. The surface observed by the SAR system is modeled by the following equation

$$z_{ij} = 3(1 - x_{ij})^2 \exp \left[ -x_{ij}^2 - (y_{ij} + 1)^2 \right] - 10 \left( \frac{x_{ij}}{5} - x_{ij}^3 - y_{ij}^5 \right) \exp \left( -x_{ij}^2 - y_{ij}^2 \right) - \frac{1}{3} \exp \left[ -(x_{ij} + 1)^2 - y_{ij}^2 \right], \quad (25)$$

where  $x_{ij} = i\Delta X$ ,  $y_{ij} = j\Delta Y$ ,  $i = \overline{1, I}$ ,  $j = \overline{1, J}$ ,  $I = 128$  pixels;  $J = 128$  pixels;  $\Delta X$ ;  $\Delta Y$  - the spatial resolution of the pixels.

Normalized amplitude of reflected signals from every pixel  $a_{ij} = 0.001$ . The spatial resolution of the pixel are  $\Delta X = \Delta Y = 2$  m. Wavelength is 0.03 m. Carrier frequency is  $3.10^9$  Hz. Frequency bandwidth is  $\Delta F = 250$  MHz. Pulse repetition period is  $T_p = 25.10^{-3}$  s. LFM pulse duration is  $T = 5.10^{-6}$  s. Sample time duration is  $\Delta T = 1, 95.10^{-8}$  s. LFM sample number is  $K = 512$ . Emitted pulse number is

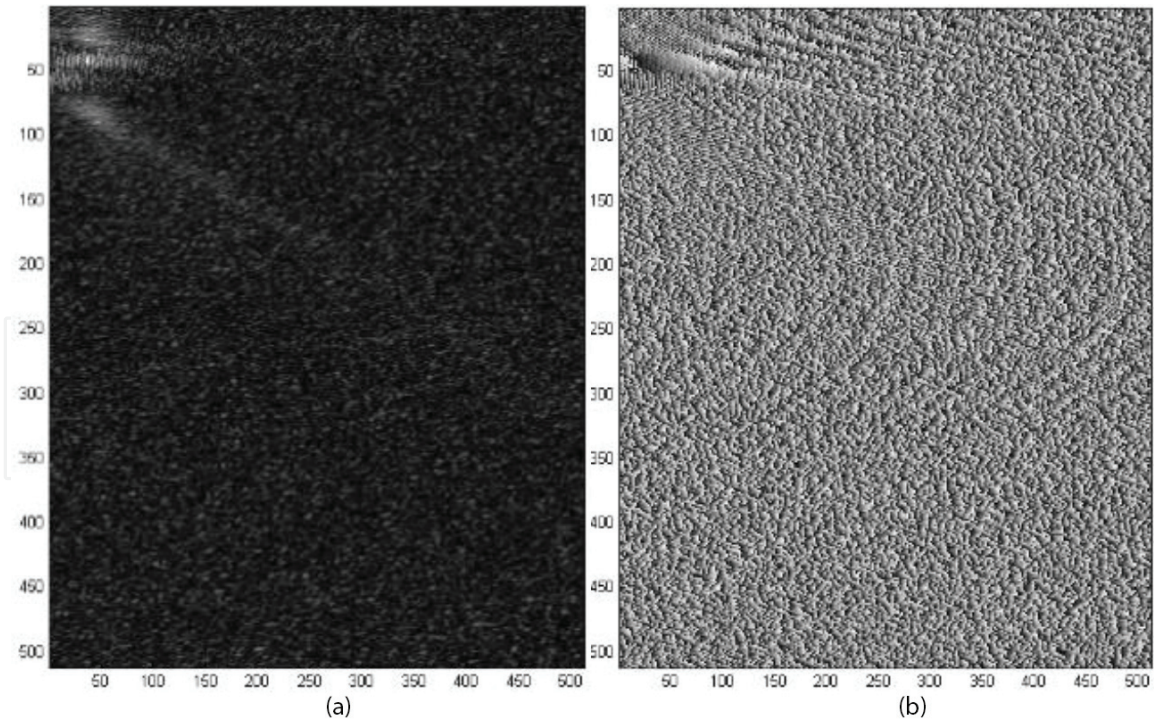


**Figure 2.**

*The real (a) and imaginary (b) component of the SAR complex signal measured in the first SAR pass.*

$M = 512$ . Digital geometry description and SAR signal modeling are performed based on the theory in Sections 3 and 4. The complex images are extracted from the SAR signal by applying correlation range compression and FFT azimuth compression. Based on a priori-known kinematical parameters of satellites and coordinates of reference point from the surface autofocusing phase correction of the SAR signals registered in the both passes can be implemented.

The real and imaginary components of the SAR complex signal measured in the first SAR pass are depicted in **Figure 2**.

The complex SAR image's amplitude and phase obtained in the first SAR pass are depicted in **Figure 3**. The orientation of the surface's image (**Figure 3a**) in the frame is defined by the position of the SAR at the moment of imaging.

The real and imaginary components of the SAR complex signal measured in the second SAR pass are depicted in **Figure 4**.

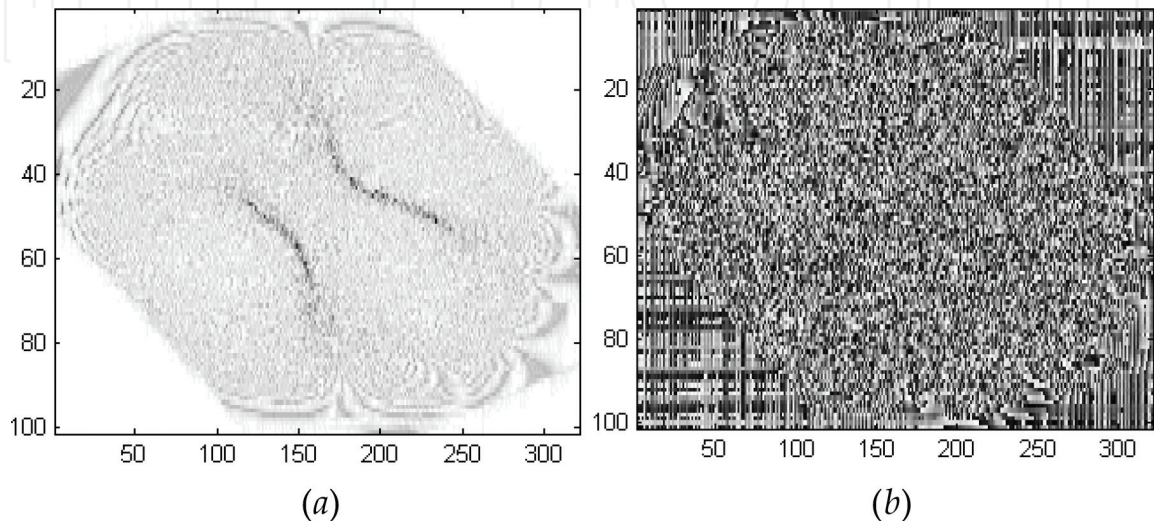


**Figure 3.**

*The amplitude (a) and phase (b) component of the SAR complex image obtained in the first pass.*

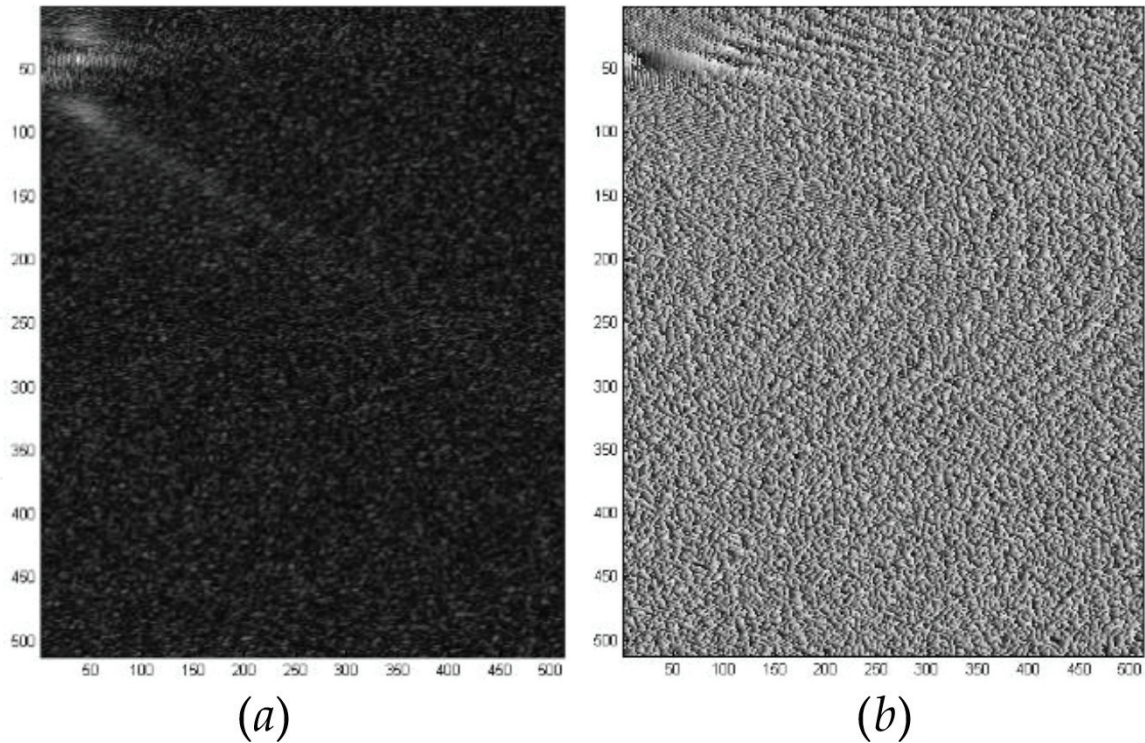


**Figure 4.**  
*The real (a) and imaginary (b) component of the SAR complex signal measured in the second SAR pass.*

The complex SAR image's amplitude and phase obtained in the second SAR pass are depicted in **Figure 5**. It can be seen that the shape of the surface (the amplitude of the complex image) is similar to the shape of the surface obtained by the first SAR pass. In contrast, the phase structures of both complex images are different based on the different SAR positions in respect of the surface in the first and second pass at the moment of imaging.

By co-registration of the first and third SAR complex images, a complex SAR interferogram can be created with components in a coherent map and interferometric phase depicted in **Figure 6**.

The real and imaginary components of the SAR complex signal obtained in the third SAR pass is depicted in **Figure 7**.

The complex SAR image's amplitude and phase obtained in the third SAR pass are depicted in **Figure 8**. The shape of the surface obtained in the third SAR pass is

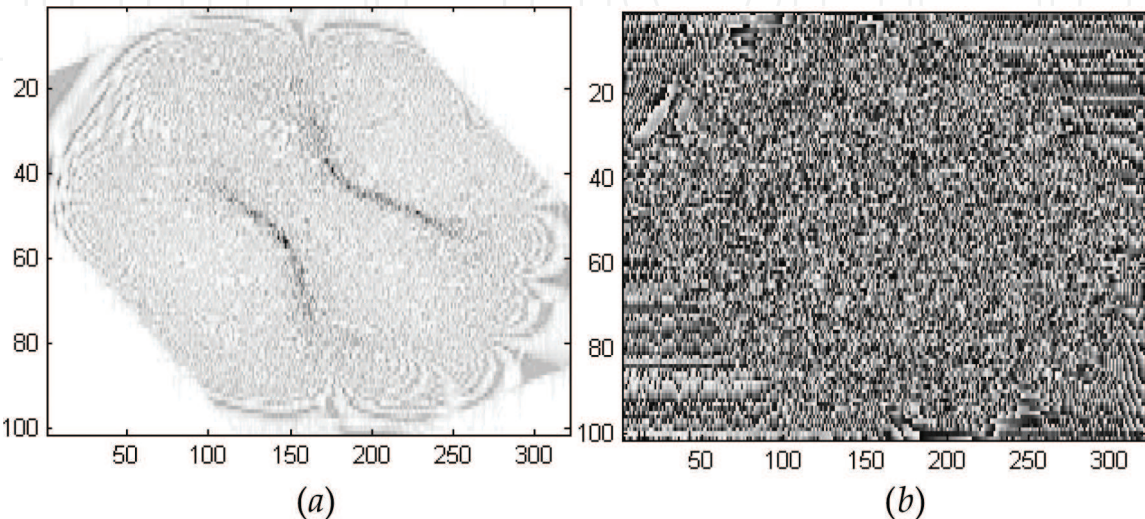


**Figure 5.**  
*The amplitude (a) and phase (b) components of the SAR complex image obtained in the second pass.*

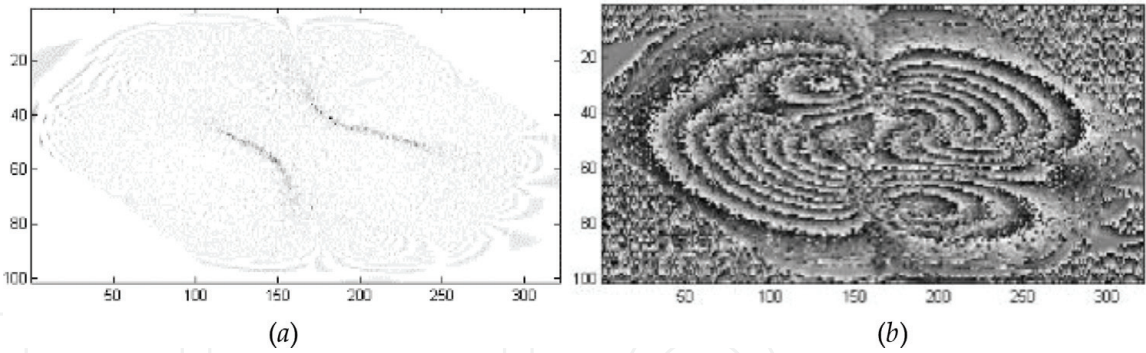


**Figure 6.**  
*The coherent map (a) and interferometric phase (b) of the complex SAR interferogram created by the first and second SAR complex images.*

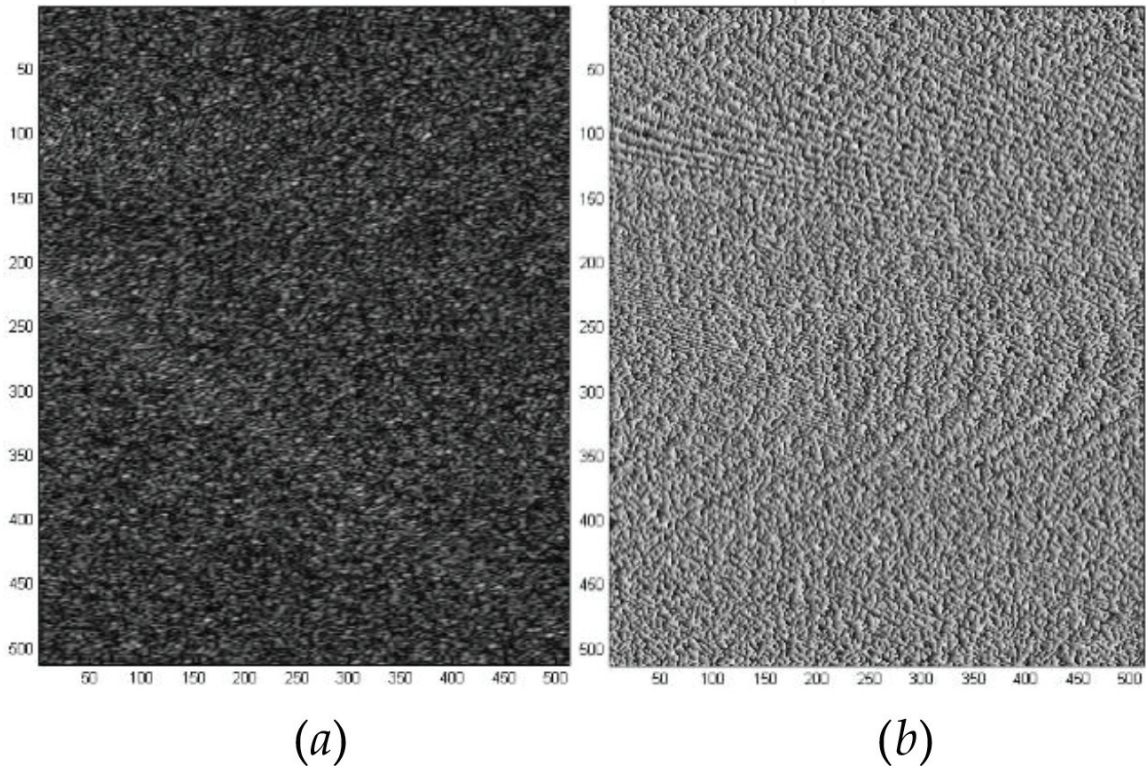


**Figure 7.**  
*The real (a) and imaginary (b) component of the SAR complex signal measured in the third SAR pass.*

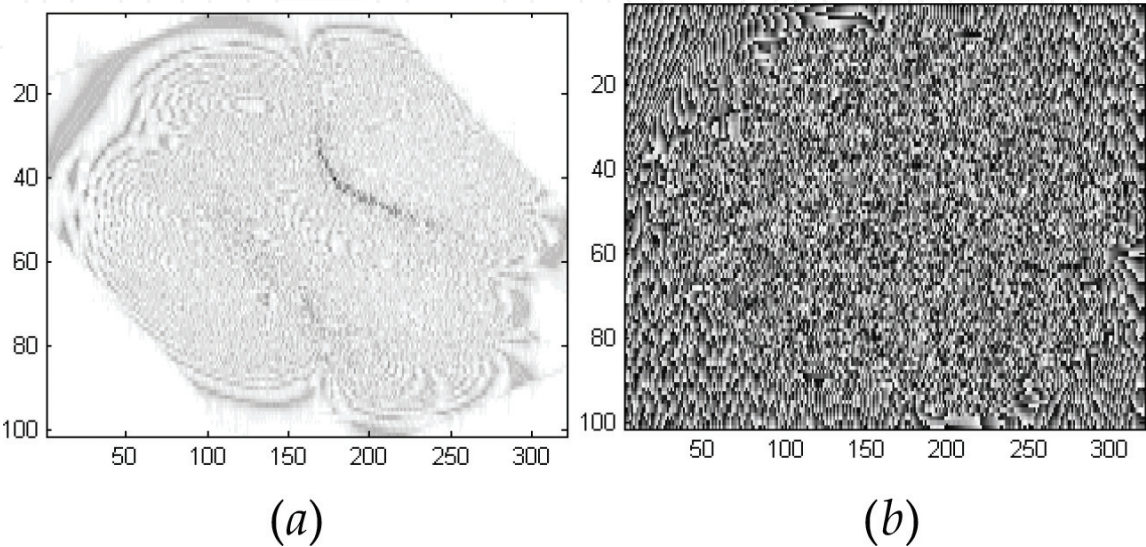


**Figure 8.**  
*The amplitude (a) and phase (b) component of the SAR complex image obtained in the third SAR pass.*

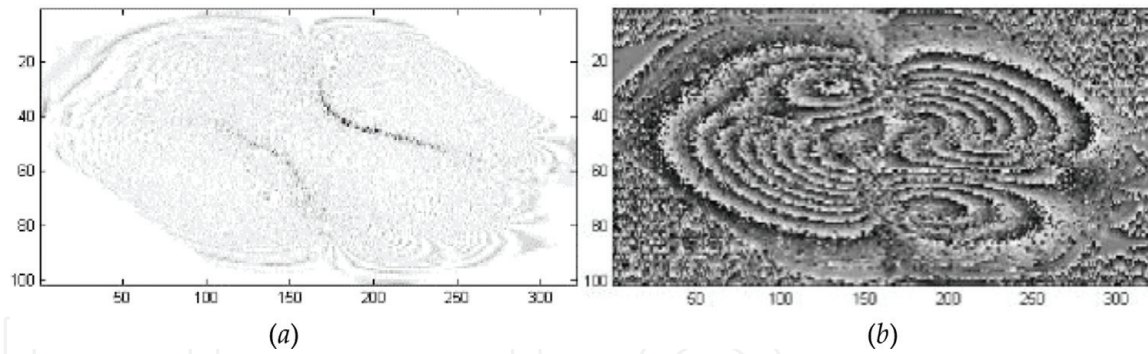


**Figure 9.** The coherent map (a) and interferometric phase (b) of the complex SAR interferogram created by the first and third SAR complex images.

similar to the shape of the surface obtained by the first and second SAR passes. Comparing phase structures of the three complex SAR images, it can be noticed that they are different based on the different SAR's positions in respect to the surface at the moment of imaging.

Under pixel co-registration of the first and third SAR complex images, a complex SAR interferogram can be created with components in a coherent map and interferometric phase depicted in **Figure 9**.

Due to precise under pixel co-registrations of the first and second and the first and third SAR complex images, the phase interferograms depicted in **Figures 6b** and **9b**, respectively, are characterized with the similar structures.

## 8. Pseudo InSAR modeling of geophysical measurements

Consider three-pass InSAR geometry (**Figure 1**). The vector distances from the SAR positions to each  $ij$ -th pixel from the region of interest are  $R_{ij}^S = R^S - R_{ij}$ , where  $S = A, B, C$  denotes the SAR position at the moment of imaging,  $R^S = [x_S, y_S, z_S]^T$  denotes the SAR vector position, and  $R_{ij} = [x_{ij}, y_{ij}, z_{ij}]^T$  denotes the  $ij$ -th pixel vector position. Coordinates of SAR positions in the moment of imaging are as follows: for a master SAR position A,  $x_A, y_A, z_A$ ; for a slave SAR position B,  $x_B, y_B, z_B$ ; and for a slave SAR position C,  $x_C, y_C, z_C$ .

After distance measurements from the master SAR position A and slave SAR positions B and C, respectively, to each  $ij$ -th pixel on the surface and co-registration of so obtained master image and slave images, the instrumental interferometric phase differences are calculated as follows

- without pixel displacement

$$\phi_{ij}^{AB} = \frac{4\pi}{\lambda} \left( |R_{ij}^A| - |R_{ij}^B| \right) - 2\pi \cdot \max \left[ \frac{2}{\lambda} \left( |R_{ij}^A| - |R_{ij}^B| \right) \right],$$

$$\phi_{ij}^{AC} = \frac{4\pi}{\lambda} \left( |R_{ij}^A| - |R_{ij}^C| \right) - 2\pi \cdot \max \left[ \frac{2}{\lambda} \left( |R_{ij}^A| - |R_{ij}^C| \right) \right]$$

- with pixel displacement

$$\phi_{ij,d}^{AC} = \frac{4\pi}{\lambda} \left( |R_{ij}^A| - |R_{ij,d}^C| \right) - 2\pi \cdot \max \left[ \frac{2}{\lambda} \left( |R_{ij}^A| - |R_{ij,d}^C| \right) \right].$$

In order to unwrap the interferometric phases, standard algorithms, MATLAB *unwrap* function, 2-D Costantini phase unwrapping based on network programming, and 2D Goldstein branch cut phase unwrapping, can be applied.

9. Pseudo InSAR geophysical measurements: numerical results

Consider a GeoTIFF file of Dilijan region in Caucasus, Armenia, located at the geographical coordinates 40° 44' 27" north and 44° 51' 47" east longitude. Consider 2-pass InSAR scenario. Coordinates of SAR positions in the moment of imaging are the following: master SAR position A,  $x_A = 0$  m,  $y_A = 300.3 \times 10^3$  m,  $z_A = 3 \times 10^5$  m and slave SAR position B  $x_B = 0$  m,  $y_B = 300 \times 10^3$  m,  $z_B = 3 \times 10^5$  m. Wavelength is 0.05 m. Distances at the moment of imaging from the SAR position A and SAR position B to each pixel on the surface are illustrated in **Figure 10a, b**. Interferogram wrapped phases and unwrapped phases are presented in **Figure 10c, d**, respectively.

Consider a three-pass InSAR scenario and a surface before (**Figure 11a**) and after (**Figure 11b**) displacement described by MATLAB function *peaks*. Coordinates of SAR positions in the moment of imaging are the following: master SAR position A,  $x_A = 350$  km,  $y_A = 350$  km,  $z_A = 800$  km; slave SAR position B  $x_B = 351.5$  km,

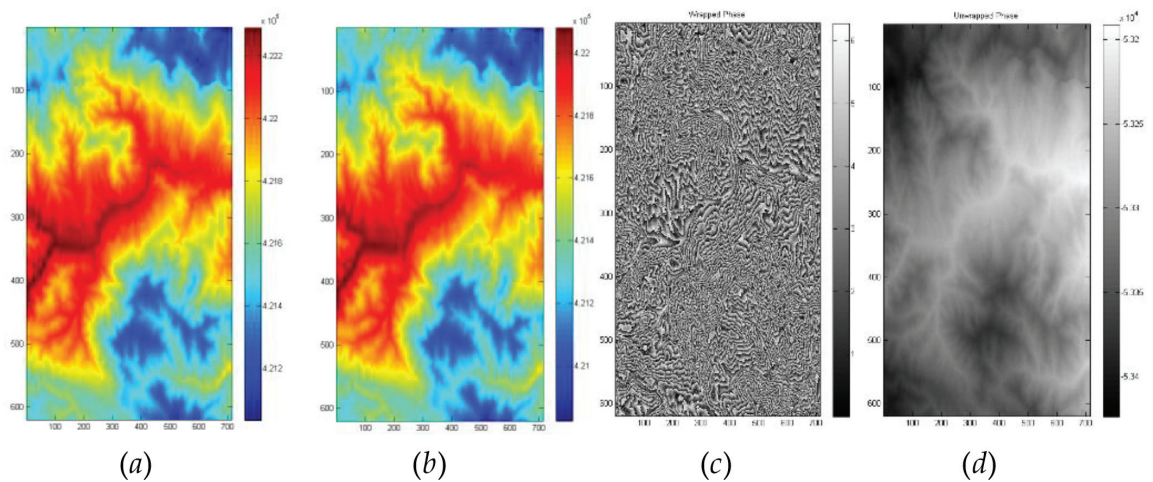


**Figure 10.** Distances from SAR position A (a) and SAR position B (b) to each pixel on the surface in pseudo color map, interferogram wrapped phases (c) and unwrapped phases (d).

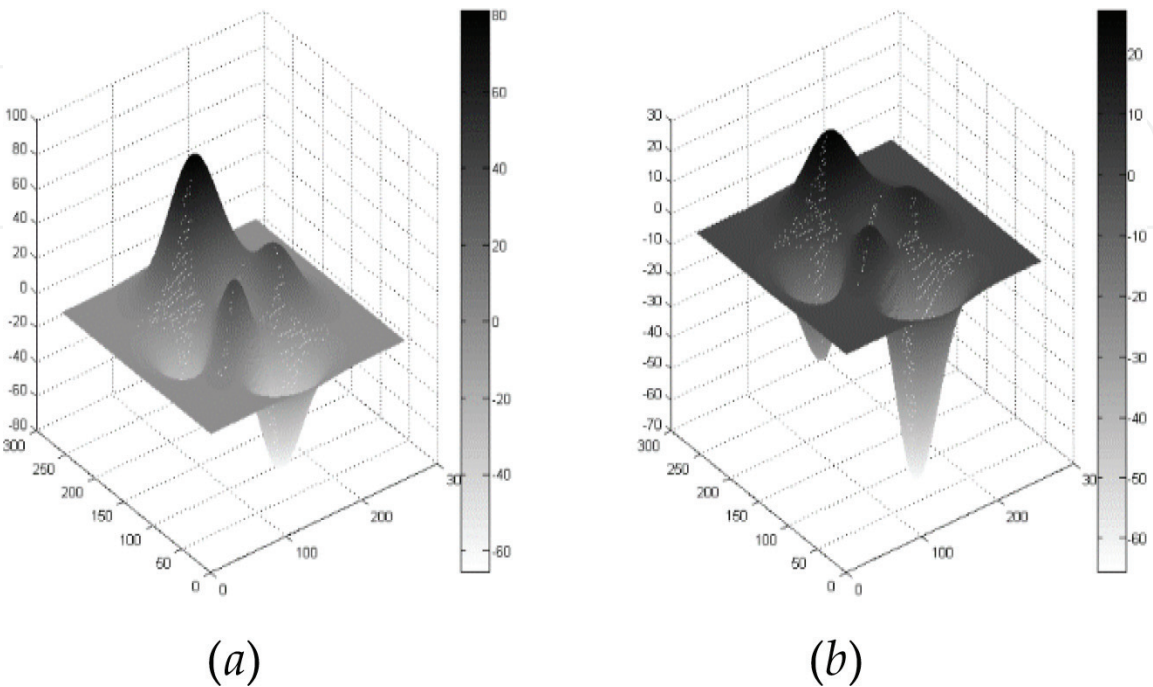


**Figure 11.** Surface (*peaks*) before (a) and after (b) displacement.

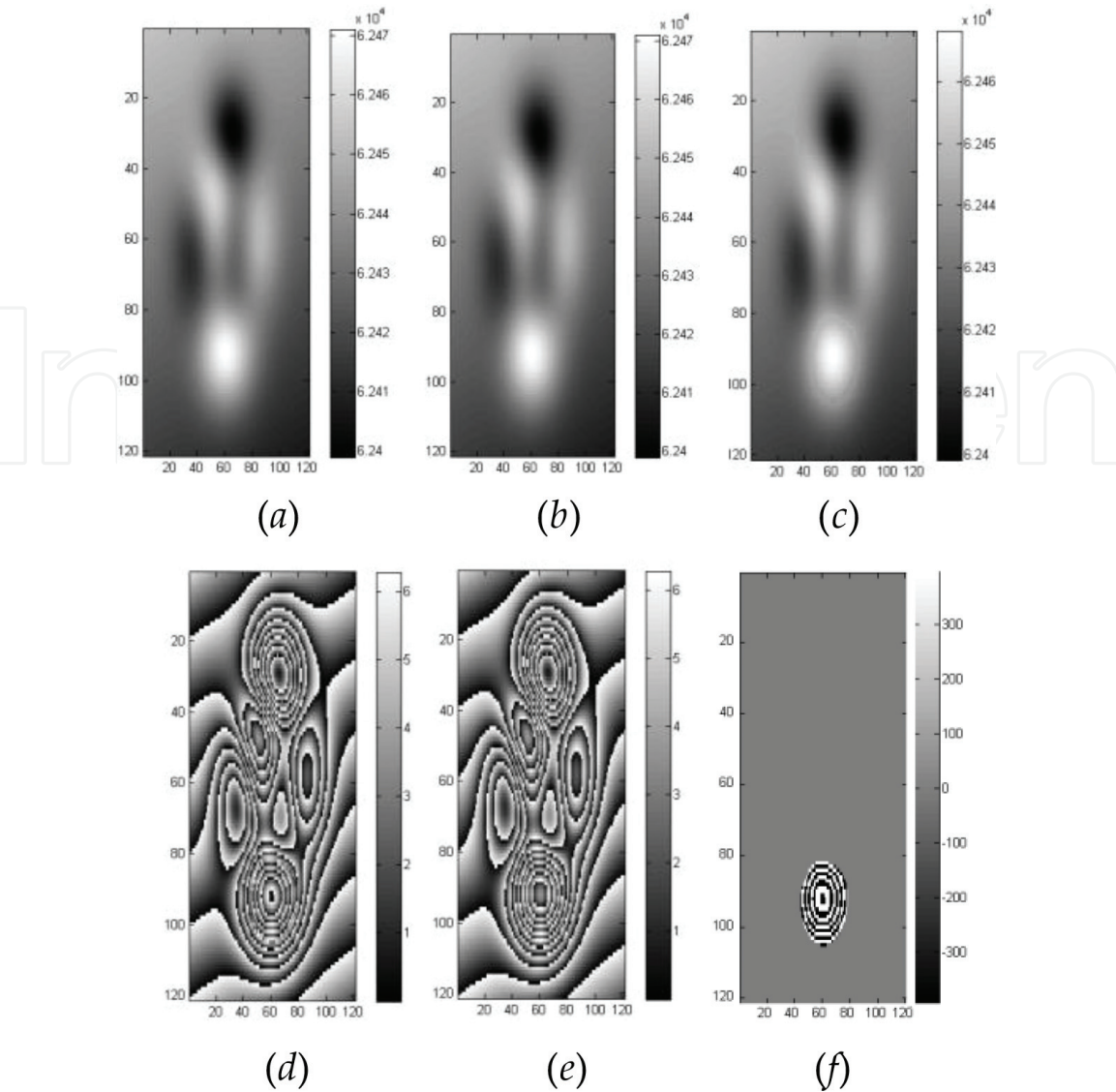


**Figure 12.** Distances to the surface measured from SAR positions A (a), B (b), and C (c). AB interferogram (d), AC interferogram (e) with surface displacement, and differential interferogram AB-AC (f).

$y_B = 350 \text{ km}$ ,  $z_B = 800 \text{ km}$ ; and slave SAR position C  $x_C = 350 \text{ km}$ ,  $y_C = 351.2 \text{ km}$ ,  $z_C = 800 \text{ m}$ . Wavelength is  $0.03 \text{ m}$ .

Distances to the surface at the moment of imaging as pseudo collar maps measured from SAR positions A, B, and C are presented in **Figure 12a–c**, respectively. AB interferogram without surface displacement and AC interferogram with surface displacement are presented in **Figure 12d, e**, respectively. Differential interferogram AB-AC is presented in **Figure 12f**.

The differential interferogram obtained by pixel subtraction of interferograms in **Figure 12d, e** is presented in **Figure 12f**. It illustrates the displacement of the surface. Only deformed part of the surface as differential fringes is depicted. The pseudo InSAR modeling can be applied to generate interferograms and differential interferograms based on real geophysical measurements and Geo TIFF maps of the observed surface.

## 10. Conclusions

A multi-pass InSAR system has been theoretically analyzed and numerically experimented. Geometry and kinematics of multi-pass InSAR scenario have been analytically described. Mathematical expressions for definition of current distance

vectors between SAR system and surface's pixels are derived. The basic InSAR parameters are defined. Analytical expressions to calculate pixel heights and pixel displacement have been derived. A model of linear frequency modulated SAR signal, reflected from the topographic surface, has been developed. An image reconstruction algorithm has been described. Numerical results verifying InSAR geometry, kinematics, and signal models are provided. Based on geometrical, kinematical, and signal models, numerical interferograms of a topographic surface have been created.

A pseudo InSAR approach has been applied to model processes of interferograms and differential interferogram generation using GeoTIFF files and measurements of distances from SAR positions to each pixels of the observed surface at the moment of imaging. Based on distance vector description of the InSAR scenario, the interferometric phase and interferometric differential phase have been analytically described. Pseudo InSAR geophysical measurements and interferograms and differential interferogram generation have been illustrated by results of numerical experiments.

In conclusion, the results in the present work can be applied for analysis and modeling of SAR interferometric processes in scenarios with different geometric, kinematics, and geological structures as well as for generating pseudo SAR interferograms based on the geophysical measurements and topographic maps.

## **Conflict of interest**

The author declares no conflict of interest.

## **Author details**

Andon Lazarov<sup>1\*</sup>, Dimitar Minchev<sup>2</sup> and Chavdar Minchev<sup>3</sup>


1 Nikola Vaptsarov Naval Academy, Vasil Drumev, Varna, Bulgaria

2 Burgas Free University, Burgas, Bulgaria

3 AADCIS Faculty, Military University, Shumen, Bulgaria

\*Address all correspondence to: [lazarov@bfu.bg](mailto:lazarov@bfu.bg)

## **IntechOpen**

© 2019 The Author(s). Licensee IntechOpen. This chapter is distributed under the terms of the Creative Commons Attribution License (<http://creativecommons.org/licenses/by/3.0>), which permits unrestricted use, distribution, and reproduction in any medium, provided the original work is properly cited. 

## References

- [1] Pepe A, Bonano M, Zhao Q, Yang T, Wang H. The use of C-/X-band time-gapped SAR data and geotechnical models for the study of Shanghai's ocean-reclaimed lands through the SBAS-DInSAR technique. *Remote Sensing*. 2016;**8**:911. DOI: 10.3390/rs8110911
- [2] Hu J, Ding X, Li Z, et al. Kalman-filter based approach for multi-sensor, multitrack and multitemporal InSAR. *IEEE Transactions on Geoscience and Remote Sensing*. 2013;**51**:4226-4239. DOI: 10.1109/TGRS.2012.2227759
- [3] Casu F, Manconi A, Pepe A, Lanari R. Deformation time-series generation in areas characterized by large displacement dynamics: The SAR amplitude pixel-offset SBAS technique. *IEEE Transactions on Geoscience and Remote Sensing*. 2011;**49**:2752-2763. DOI: 10.1109/TGRS.2010.2104325
- [4] Samsonov S, d'Oreye N. Multidimensional time-series analysis of ground deformation from multiple InSAR data sets applied to Virunga Volcanic Province. *Geophysical Journal International*. 2012;**191**:1095-1108. DOI: 10.1111/j.1365-246X.2012.05669.x
- [5] Sansosti E, Berardino P, et al. How second-generation SAR systems are impacting the analysis of ground deformation. *International Journal of Applied Earth Observation and Geoinformation*. 2014;**28**:1-11. DOI: 10.1016/j.jag.2013.10.007. Available from: <https://www.sciencedirect.com/science/article/pii/S0303243413001323> [Accessed: 11 August 2019]
- [6] Vettore A, Ponte S, et al. Space-based surface change detection with differential Synthetic Aperture Radar (SAR) Interferometry: Potentialities and preliminary investigations. In: *Symposium on Geospatial Theory, Processing and Applications*; Ottawa; 2002. Available from: <https://www.semanticscholar.org/paper/Space-based-surface-change-detection-with-Synthetic-Ponte-Crocetto/10591de3ab1c236a30f2eeaff3ab1f3e8da1af17> [Accessed: 11 August 2019]
- [7] Wang J, Yu W, Deng Y, Wang R, et al. Demonstration of time-series InSAR processing in Beijing using a small stack of Gao-fen-3 differential interferograms. *Journal of Sensors*. 2019;**2019**:4204580. DOI: 10.1155/2019/4204580
- [8] Pepe A, Calò F. Review of interferometric synthetic aperture radar (InSAR) multi-track approaches for the retrieval of Earth's surface displacements. *Applied Sciences*. 2017;**7**:1264. DOI: 10.3390/app7121264
- [9] Fuhrmann T, Garthwaite M, Lawrie S, Brown N. Combination of GNSS and InSAR for future Australian datums. In: *International Global Navigation Satellite Systems Association IGNS Symposium 2018*; Colombo Theatres, Kensington Campus, UNSW Australia; 7-9 February 2018. Available from: [http://www.ignss2018.unsw.edu.au/sites/ignss2018/files/u80/Papers/IGNSS2018\\_paper\\_17.pdf](http://www.ignss2018.unsw.edu.au/sites/ignss2018/files/u80/Papers/IGNSS2018_paper_17.pdf) [Accessed: 11 August 2019]
- [10] Xinshuang W, Lingling L, Xiaoliang Sh, Xitao H, Weil G. A high precision DEM extraction method based on InSAR data. In: *ISPRS Annals of the Photogrammetry, Remote Sensing and Spatial Information Sciences*, Volume IV-3, 2018 ISPRS TC III Mid-Term Symposium "Developments, Technologies and Applications in Remote Sensing", 7-10 May, Beijing, China; 2018. Available from: <https://pdfs.semanticscholar.org/7f92/aca4273b2afb1b9347724d72eb4c13bcd1cc.pdf> [Accessed: 10 August 2019]
- [11] Crosetto M, Crippa B. Quality assessment of interferometric SAR DEMs. In: *International Archives of*

- Photogrammetry and Remote Sensing. Vol. XXXIII, Part B1; Amsterdam; 2000. Available from: <https://pdfs.semantic-scholar.org/376f/4f7f12602827801b954c7fb79aae2585b9c3.pdf> [Accessed: 28 July 2019]
- [12] Letsios V, Faraslis I, Stathakis D. InSAR digital surface model (DSM) using Sentinel 1 and spatial data creation. In: AGILE 2019—Limassol; June 17–20, 2019. Available from: [https://agile-online.org/images/conference\\_2019/documents/short\\_papers/50\\_Upload\\_your\\_PDF\\_file.pdf](https://agile-online.org/images/conference_2019/documents/short_papers/50_Upload_your_PDF_file.pdf) [Accessed: 28 July 2019]
- [13] Liang C, Agram P, Simons M, Fielding EJ. Ionospheric correction of InSAR time series analysis of C-band Sentinel-1 TOPS data. This paper is a non-peer reviewed preprint published at EarthArXiv and submitted for consideration by IEEE TGRS. DOI: 10.1109/TGRS.2019.2908494. Available from: <https://eartharxiv.org/atxr7/download>
- [14] Li Z, Bethel J. DEM registration, alignment and evaluation for SAR interferometry. In: The International Archives of the Photogrammetry, Remote Sensing and Spatial Information Sciences. Vol. XXXVII. Part B1. Beijing; 2008. pp. 11-116. Available from: [https://www.isprs.org/proceedings/XXXVII/congress/1\\_pdf/19.pdf](https://www.isprs.org/proceedings/XXXVII/congress/1_pdf/19.pdf) [Accessed: 07 August 2019]
- [15] Mao W-J, Chang W-L. Deformation monitoring by ground-based SAR interferometry (GB-InSAR): A field test in dam. *Advances in Information Sciences and Service Sciences (AISS)*. 2015;7(2):133-140. Available from: <http://www.globalcis.org/aiss/ppl/AISS3808PPL.pdf> [Accessed: 05 August 2019]
- [16] Liu D, Chen R, Riedel B, Niemeier W. An improved approach to estimate large-gradient deformation using high resolution TerraSAR-X data. *Solid Earth Discussions*. 2014;6: 2759-2778. DOI: 10.5194/sed-6-2759-2014. Available from: <https://www.solid-earth-discuss.net/6/2759/2014/sed-6-2759-2014.pdf> [Accessed: 01 August 2019]
- [17] Fattahi H, Simons M, Agram P. InSAR time-series estimation of the ionospheric phase delay: An Extension of the split Range-Spectrum technique. *IEEE Transactions on Geoscience and Remote Sensing*. 2017;55(2):777-786. Available from: [http://web.gps.caltech.edu/~simons/publications/pdfs/Fattahi\\_2017.pdf](http://web.gps.caltech.edu/~simons/publications/pdfs/Fattahi_2017.pdf) [Accessed: 01 August 2019]
- [18] Sosnovsky A, Kobernichenko V, Vinogradova N, Tsogtbaatar Ol. InSAR data coherence estimation using 2D fast Fourier transform. *CEUR Workshop Proceedings (CEUR-WS.org)*. 2017; 1814:98-105. Available from: <http://ceur-ws.org/Vol-1814/paper-12.pdf> [Accessed: 10 August 2019]